Research Article

Corrosion engineering boosting bulk Fe$_{50}$Mn$_{30}$Co$_{10}$Cr$_{10}$ high-entropy alloy as high-efficient alkaline oxygen evolution reaction electrocatalyst

Pengfei Zhou[a], Dong Liu[a], Yuyun Chen[a], Mingpeng Chen[a], Yunxiao Liu[b], Shi Chen[a], Chi Tat Kwok[c], Yuxin Tang[d,**], Shuangpeng Wang[a,b,*], Hui Pan[a,b,*]

[a] *Institute of Applied Physics and Materials Engineering, University of Macau, 999078, Macao*
[b] *Department of Physics and Chemistry, Faculty of Science and Technology, University of Macau, 999078, Macao*
[c] *Department of Electromechanical Engineering, Faculty of Science and Technology, University of Macau, 999078, Macao*
[d] *College of Chemical Engineering, Fuzhou University, Fuzhou 350116, China*

A B S T R A C T

Oxygen evolution reaction (OER) is a critical process in electrocatalytic water splitting. However, the development of low-cost, highly efficient OER electrocatalysts by a simple method that can be used for industrial application on a large scale is still a huge challenge. Recently, high entropy alloy (HEA) has acquired extensive attention, which may provide answers to the current dilemma. Here, we report bulk Fe$_{50}$Mn$_{30}$Co$_{10}$Cr$_{10}$, which is prepared by 3D printing on a large scale, as electrocatalyst for OER with high catalytic performance. Especially, an easy approach, corrosion engineering, is adopted for the first time to build an active layer of honeycomb nanostructures on its surface, leading to ultrahigh OER performance with an overpotential of 247 mV to achieve a current density of 10 mA cm^{-2}, a low Tafel slope of 63 mV dec^{-1}, and excellent stability up to 60 h at 100 mA cm^{-2} in 1 M KOH. The excellent catalytic activity mainly originates from: (1) the binder-free self-supported honeycomb nanostructures and multi-component hydroxides, which improve intrinsic catalytic activity, provide rich active sites, and reduce interfacial resistance; and (2) the diverse valence states for multiple active sites to enhance the OER kinetics. Our findings show that corrosion engineering is a novel strategy to improve the bulk HEA catalytic performance. We expect that this work would open up a new avenue to fabricate large-scale HEA electrocatalysts by 3D printing and corrosion engineering for industrial applications.

© 2022 Published by Elsevier Ltd on behalf of The editorial office of Journal of Materials Science & Technology.

1. Introduction

Electrochemical water splitting to produce hydrogen and oxygen is one of the most promising and appealing strategies for converting renewable energy to chemical fuel with high energy density to meet the energy demand [1–4]. The overall water splitting can be divided into two half-reactions: the cathodic hydrogen evolution reaction (HER, two-electron process) and the anodic oxygen evolution reaction (OER, four-electron process) [5,6]. The OER process is the rate-determining half-reaction in water

splitting due to its intrinsically complex, multiple proton/electron-coupled steps [7,8]. Hence, high-efficient OER electrocatalysts are desired to enhance the energy conversion efficiency by improving the reaction kinetics and lowering the overpotential. Although iridium/ruthenium oxides (IrO$_2$/RuO$_2$) are regarded as the state-of-the-art electrocatalysts for OER [9], they are precious and limited on earth, which has greatly hindered their large-scale commercial applications [10].

To date, numerous no-precious-metal-based catalytic materials have been studied for OER, such as oxides/(oxy)hydroxides [11,12], hydroxides [13–15], sulfides/selenides [16,17], phosphides [18,19], and nitrides [20]. For example, Liu et al. reported that the trimetallic nitride compound grown on nickel foam (CoVFeN @ NF) showed an ultralow OER overpotentials of 212 and 264 mV at 10 and 100 mA cm^{-2} in 1 M KOH, respectively [20]. Most of these reported catalysts showed highly efficient catalytic activity and excellent stability. However, they were powders or grown on the Ni

foam or carbon cloth, which were fabricated by a complicated process and couldn't be for the on-large-scale production, leading to difficulty for industrial applications. Therefore, exploring and developing self-supported OER catalysts with excellent performance on-large scale in a simple way is still a challenge [21].

In the past decade, high entropy alloy (HEA) has attracted increasing attention for its applications in the conventional structure materials field because of its intriguing properties, including high hardness and compressive strength, and good creep/wear/corrosion/oxidation resistance [22–27]. Particularly, HEA with controllable size can be achieved by advanced 3D printing, which promotes wider applications [22,28]. As HEA is composed of multiple transition metals, such as Fe, Co, Ni, Mn, and Mo, which are commonly used as electrocatalysts for water splitting [29,30], it has been recently explored for applications into energy conversion [31,32]. Based on the synergistic effect of different elements, the HEA nanoparticles containing noble metal have been widely studied as catalysts for energy conversion [31,33–35]. Despite the HEA nanoparticles with noble metal showed efficient performance, they have relatively high cost, which restricts their practical application. Nowadays, the non-precious metal based HEA powders were also studied for catalysis [29,36]. For example, Dai et al. reported that MnFeCoNi exhibited an excellent OER performance comparable to or even better than RuO_2 [37]. Although the performances of nanoscale HEA powders obtained by mechanical alloying [37], one-pot solvothermal reaction [38], or dealloying method [39–41] were improved, they can detach easily from the support in the OER process, leading to similar disadvantages as other powders, such as instability and small-scale electrode, which is unsuitable for practical applications. Bulk HEA has prospective as highly efficient, stable, and large-scale catalysts for OER in industrial water splitting. However, the bulk HEAs show poorer OER performance than nanomaterials [42]. Therefore, it is necessary to improve the OER performance of bulk HEA.

Corrosion engineering is an effective method to increase the active sites and improve the catalytic performance of alloy, which only changes its surface [43–45]. Liu et al. reported that the nanosheet arrays consisted of iron-containing layered double hydroxides on the iron substrate were obtained via the corrosion in the $NiSO_4$ solution, which showed excellent catalytic activities and stability for over 6000 h at 1000 mA cm^{-2} [43]. Hence, corrosion engineering is a very effective, inexpensive, and simple method to prepare self-supported catalysts, which should be much suitable for large-scale commercial applications. To the best of our knowledge, corrosion engineering has not been used to prepare the self-supported HEA catalysts for OER.

In this study, we use different sulfates to corrode the surface of $Fe_{50}Mn_{30}Co_{10}Cr_{10}$ prepared by the 3D printing technology. We find that honeycomb nanostructures are formed by the corrosion engineering, resulting in improved OER catalytic performance. The self-supported HEA shows an excellent performance for OER with overpotentials of 247, 313, and 362 mV to achieve the current densities of 10, 50, and 100 mA cm^{-2} in 1 M KOH, respectively, as well as a small Tafel slope of 63 mV dec^{-1} and excellent stability for 60 h under 100 mA cm^{-2}.

2. Experiment section

2.1. Preparation of $Fe_{50}Mn_{30}Co_{10}Cr_{10}$ bulk HEA

The metastable dual-phase $Fe_{50}Mn_{30}Co_{10}Cr_{10}$ (at.%) was prepared by selective laser melting (SLM) process using gas atomized HEA powders. The SLM processing was performed at room temperature using an FS271 facility (Farsoon, Inc, China) equipped with a 500 W Gaussian beam fiber laser with a focused laser beam diameter of 90 μm under high purity Ar atmosphere. The large blocks

with the dimension of $30 \times 10 \times 10$ mm^3 were produced. The laser power (P) was 400 W, the scan speed (v) was 1200 mm/s, the scan interval (h) was 0.09 mm, and the layer thickness (t) was 30 μm. Then, the bulk HEA was cut into pieces with a size of $1 \times 10 \times 10$ mm^3 by electrical discharge machining for corrosion treatment.

2.2. Preparation of HEA catalysts

The prepared bulk HEA was corroded for 24 h at room temperature under different sulfate solutions, including 250 mM $NiSO_4$, 250 mM $CoSO_4$, 250 mM $FeSO_4$, the mixed solution of 125 mM $NiSO_4$ and 125 mM $CoSO_4$, and the mixed solution of 125 mM $NiSO_4$ and 125 mM $FeSO_4$. For comparison, we also tried different concentrations of $NiSO_4$ to treat the HEA for 24 h. The catalysts treated under different sulfates and different concentrations of $NiSO_4$ were labeled as HEA (without treatment), HEA-250Ni (250 mM $NiSO_4$), HEA-250Co (250 mM $CoSO_4$), HEA-250Fe (250 mM $FeSO_4$), HEA-125Ni-125Co (mixed solution of 125 mM $NiSO_4$ and 125 mM $CoSO_4$), HEA-125Ni-125Fe (mixed solution of 125 mM $NiSO_4$ and 125 mM $FeSO_4$), HEA-100Ni (100 mM $NiSO_4$), HEA-500Ni (500 mM $NiSO_4$), and HEA-1000Ni (1000 mM $NiSO_4$), respectively.

2.3. Materials characterization

The X-ray diffraction (XRD) was performed on Rigaku Smartlab X-ray diffractometer with Cu Kα radiation, with a scan rate of 2 degree/min. Raman signal measurement was performed on a Micro Raman System (Horiba LABHRev-UV) under the excitation sources of 532 nm. A scanning electron microscopy (SEM) test was performed on a Zeiss Sigma instrument to observe the morphology of the samples. Transmission electron microscopy (TEM) and high-resolution transmission electron microscopy (HRTEM) were carried out on Tecnai G2 F30 at 200 kV. X-ray photoelectron spectroscopy (XPS, Thermo Fisher Scientific) with Al Kα X-ray (hν = 1486.7 eV) was used to analyze the chemical compositions and valence states of elements.

2.4. Electrochemical measurements

The electrocatalytic performance was tested on an electrochemical workstation (ModuLab XM) in 1 M KOH at room temperature, where the self-supported HEA, Hg/HgO (1 M KOH), and graphite rod were used as the working, reference, and counter electrodes, respectively. To obtain the stable test, the sample was pre-activated for 500 cycles through cyclic voltammetry (CV) at the scan rate of 300 mV/s. The linear sweep voltammetry (LSV) polarization curves were measured from high initial potential to low potential (negative scan) to avoid the overlap of the oxidation and OER signals. The scan rate for LSV was 2 mV s^{-1} and LSV curves with and without automatically iR compensation (80%) were obtained by applying the current interrupt method. The real potential values for OER were calculated using the Nernst equation (a reference to the reversible hydrogen electrode (RHE)): $E_{RHE} = E_{Hg/HgO} + 0.098 + 0.0591 \times$ pH, where the measured pH value is 13.71. For evaluating the double-layer capacitance of the catalysts, the CV curves were measured with various scan rates (20, 40, 60, 80, and 100 mV s^{-1}) under the potential window of 0.1–0.2 V vs. Hg/HgO in 1 M KOH. Electrochemical impedance spectroscopy (EIS) measurements were accomplished on an electrochemical workstation (ModuLab XM) at a potential of 0.65 vs. Hg/HgO with a frequency range of 10^{-2}–10^5 Hz in 1 M KOH solution. For comparison, the Ni foam was also tested for OER. The long-term stability test for OER was carried out at a constant potential of 0.725 V vs. RHE for 60 h without iR correction.
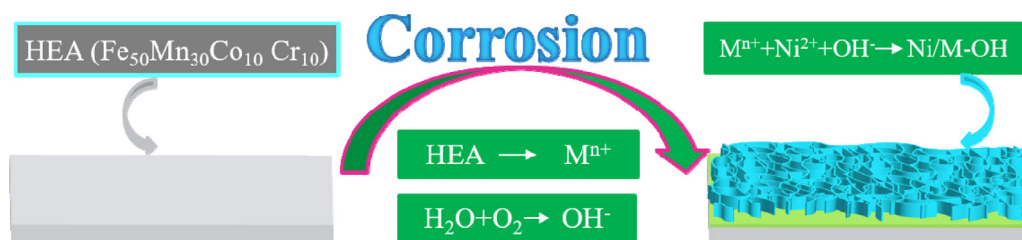
Scheme 1. Schematic illustration for the formation of the nanostructure on HEA surface via corrosion engineering.
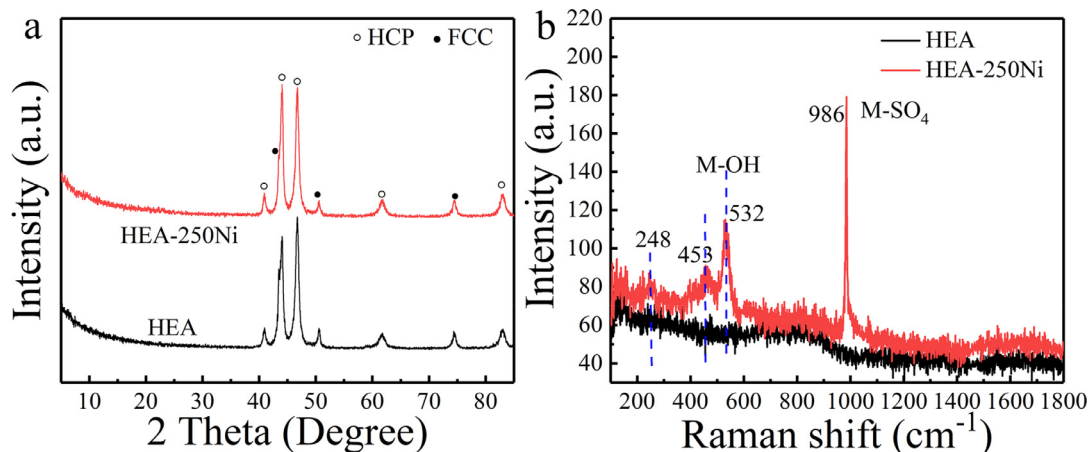

Fig. 1. (a) XRD patterns and (b) Raman spectra of the HEA with and without corrosion in 250 mM NiSO$_4$.

3. Results and discussion

3.1. The formation of nanostructures on the HEA surface via corrosion engineering

When an alloy exposes to humid air, oxides/hydroxides unavoidably form on its surface due to corrosion, which can be active species to promote the OER process [43–45]. Here, the HEA sheet was immersed in the aqueous solutions containing a certain amount of divalent cations (e.g. Ni^{2+}, Co^{2+}, Fe^{2+}, or their mixture) at room temperature. The multi-metal hydroxides are spontaneously generated on the HEA surface due to the intentional introduction of divalent cations in the corrosive environment. The M^{n+} (M = Fe, Co, Cr, Mn; n = 2, 3, etc.) ions on the HEA surface react with the cations of sulfates, such as Ni^{2+}, and OH$^-$ to form multi-metal hydroxides on the interface of the HEA sheet and the solution, resulting in the formation of hydroxides on the HEA surface (Scheme 1).

3.2. XRD and Raman signals of the samples

The XRD patterns show that Fe$_{50}$Mn$_{30}$Co$_{10}$Cr$_{10}$ mainly consists of two phases, namely FCC (face-centered cubic) and HCP (hexagonal close-packed) phases (Fig. 1(a)), which is consistent with the literature [23]. After the corrosion in 250 mM NiSO$_4$, no new phase is obviously detected in HEA-250Ni. The Raman spectrum shows that there is no obvious signal for the HEA due to its metallic nature (Fig. 1(b)). Interestingly, there are a few peaks detected on HEA-250Ni, indicating the formation of new materials or contaminations. The peaks at 248, 453 and 532 cm^{-1} indicate the hydroxides, and the peak at 986 cm^{-1} is related to the sulfates. Therefore, we see that a certain amount of hydroxides is achieved after the corrosion in 250 mM NiSO$_4$, which cannot be detected by XRD due to its detection limit.

3.3. Morphology of the catalysts

To confirm the formation of nanostructures, the surface morphology of HEA with and without corrosion was examined by SEM. The SEM images show that there is no obvious morphology on HEA before the corrosion (Figs. 2(a) and S1(a) and (b) in Supporting Information). Interestingly, a layer of honeycomb nanostructures is observable on the HEA surface after the corrosion (Figs. 2(b) and (c), and S1 in supporting information). We see that the formation of multi-metal hydroxides on HEA depends on the concentration and the types of sulfates. Only a small part of HEA could be corroded into honeycomb nanostructures under a low concentration of NiSO$_4$ (100 mM) (Fig. S1(c), supporting information). With the concentration of NiSO$_4$ increased to 250 mM, most of the HEA surface could be corroded into honeycomb nanostructures, which distribute uniformly (Figs. 2(b) and (c), and S1(d) in supporting information). Large particles are obtained, when the concentration of NiSO$_4$ is over 500 mM (Fig. S1(e) and (f), supporting information). Different sulfate solutions have different effects on the morphology of the HEA (Fig. S2, supporting information). Generally, the relatively uniform honeycomb nanostructures are formed as 250 mM CoSO$_4$ is used, but its uniformity is poorer than that of HEA-250Ni. At the same time, the honeycomb nanostructures obtained in 250 mM CoSO$_4$ are bigger than those of HEA-250Ni (Fig. S2(c), supporting information). The mixture of CoSO$_4$ and NiSO$_4$ can also promote the formation of honeycomb nanostructures with the honeycomb size between those of CoSO$_4$ and NiSO$_4$, indicating that CoSO$_4$ is more conducive to the formation of honeycomb structures, but not uniformly (Fig. S2(e), supporting information). Only dense nanoparticles can be observed on the HEA corroded by 250 mM FeSO$_4$ and the mixture of FeSO$_4$ and NiSO$_4$, indicating that the FeSO$_4$ solution cannot help the honeycomb nanostructures form on the HEA surface (Fig. S2(d) and (f), supporting information).
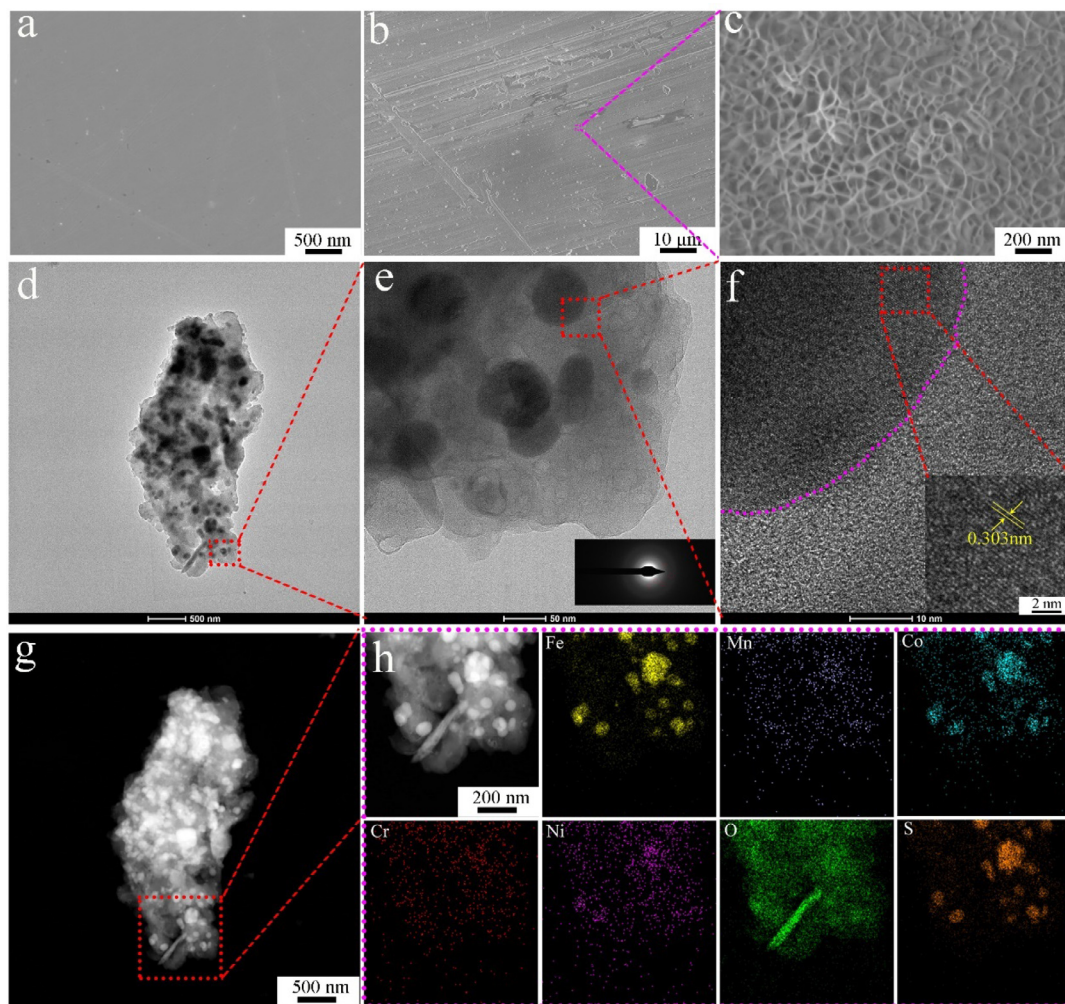
Fig. 2. (a) SEM image of HEA. (b) and (c) SEM images, (d)-(f) HRTEM images, and (g) and (h) EDS mappings of HEA-250Ni.

To further analyze the nanostructures on the corroded HEA, high-resolution transmission electron microscopy (HRTEM) was used. We see that the nanostructures on the HEA-250Ni surface consist of nanosheets with some nanoparticles decorated (Fig. 2(d) and (e)). The selected area electron diffraction (SAED) patterns reveal that the nanostructures are amorphous and the nanoparticles show crystalline characteristics (Fig. 2(e), inset), which are further confirmed by the HRTEM image (Fig. 2(f)). The HADDF-STEM images and EDS mappings (Fig. 2(g) and (h)) show that the nanosheets are mainly composed of Mn, Co, Cr, Ni, and O, while the nanoparticles are dominated by Fe, Co, Ni, O, and S. The EDS mapping and Raman patterns demonstrate that the nanosheets are mainly amorphous multi-metal hydroxides, and the nanoparticles are the residual multi-metal sulfates. The amorphous multi-metal hydroxides formed in the sulfate solution may be contributed to the abundant metal cations that can meet the basic structure of amorphous hydroxides, and the weak acidic sulfates solution that is suitable for the formation of amorphous hydroxides [43].

3.4. XPS analysis

X-ray photoelectron spectroscopy (XPS) was further employed to characterize the surface chemical states of HEA (Fig. S3, supporting information) and HEA-250Ni (Fig. 3). The XPS fine spectra of Fe 2p, Mn 2p, Co 2p, Cr 2p, and Ni 2p shows the $2p_{3/2}$ and $2p_{1/2}$ doublets because of the spin-orbit coupling (Figs. 3 and S3 in

supporting information). Except for the satellite peaks (green lines, denoted as "Sat."), the spectra of Fe, Mn, Co, and Cr elements of HEA can be deconvolved into three types of peaks, which correspond to the metal peak (red lines), oxide peak (blue lines) and hydroxide peak (pink lines) (Fig. S3(a)–(d), Supporting Information). For example, the peaks at 706.6 and 707.5 eV are assigned to the Fe metal with different phases [36], because Fe in the two phases (FCC and HCP) has a slight difference in XPS. The peaks at about 710.2 and 711.8 eV are associated with Fe-OH and Fe-O, respectively (Fig. S3(a), supporting information) [7, 46]. The other two peaks at 713.6 and 715.5 eV are corresponding to satellite peaks. The O 1s spectra exhibit two characteristic peaks, corresponding to the lattice oxygen-metal (529.7 eV) and hydroxyl groups (531.5eV) (Fig. S3(f), supporting information), respectively [46,47]. The XPS spectra of HEA reveals that there are some hydroxides and oxides on the HEA surface due to the corrosion in air. For HEA-250Ni, except for the satellite peaks, Fe mainly shows three kinds of peaks, namely the Fe metal (707.5 eV), hydroxides (710.5 eV), and some sulfates (712.9 eV, light blue line) (Fig. 3(a)) [48]. However, different from Fe, the $P_{1/2}$ and $P_{3/2}$ peaks of Mn and Co elements could not be separated (Fig. 3(b) and (c)), which may be due to the complex composition of the HEA-250Ni surface. The $P_{1/2}$ and $P_{3/2}$ peaks of Co could be affected by the Ni LM_8 and Fe LM_2 peaks, and those of Mn are affected by the Ni LM_2 peaks. In addition, the Cr signal cannot be detected after the corrosion engineering (Fig. 3(d)), indicating that most of the Cr atom on the sur-
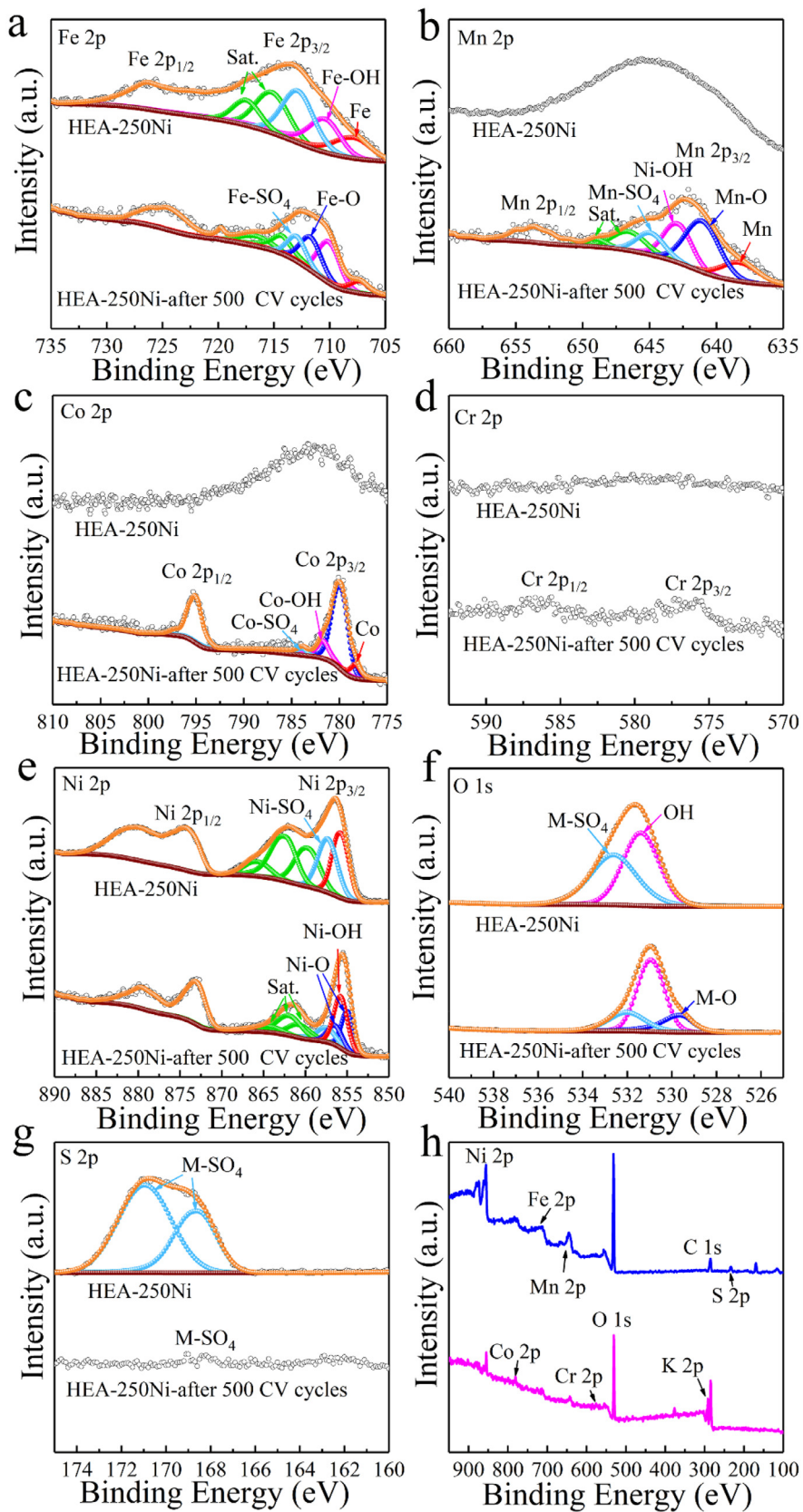
Fig. 3. High-resolution XPS spectra of (a) Fe 2p, (b) Mn 2p, (c) Co 2p, (d) Cr 2p, (e) Ni 2p, (f) O 1s, and (g) S 2p, and (h) survey XPS spectrum for HEA-250Ni before and after 500 CV cycles.

face of HEA is dissolved into the solution [49]. For the Ni element, the two main peaks of Ni-SO$_4$ (857.4 eV, light blue line) [50] and Ni-OH (855.8 eV, pink line) [51] are observed except for the satellite peaks (859.8, 862.5, and 865.9 eV, green lines) (Fig. 3(e)), and the O element also shows the OH-M (531.4 eV) and SO$_4$_M peaks (532.6 eV) (Fig. 3(f)), as well as the S element for the SO$_4$_M peaks (168.6 and 170.9 eV) [52,53] (Fig. 3(g)). Therefore, we conclude that HEA-250Ni is mainly composed of metal, hydroxides, and sulfates, which is consistent with the TEM results. As OER is carried out in alkaline solution, we investigate the effect of the OER test on the surface chemical composition, and the XPS for HEA-250Ni after the CV activation for 500 cycles was tested. We can see clearly that the P$_{1/2}$ and P$_{3/2}$ peaks for Mn and Co are detected after the CV activation (Figs. 3(b) and (c)), indicating that the surface reconstruction of the nanostructures on HEA-250Ni. For the Fe, Mn, and Co elements, a few new peaks of oxides (Fe-O: 711.7; Mn-O: 641.1; Co-O: 780.0 eV) are detected, except for the metals (Fe: 707.2; Mn: 638.3; Co: 778.3 eV), hydroxides (Fe-OH: 710.2; Mn-OH: 643.0; Co-OH: 781.6 eV), and a small number of sulfates (Fe-SO$_4$: 713.1; Mn-SO$_4$: 645.0; Co-SO$_4$: 783.9 eV) (Fig. 3(a)–(c)). The weak Cr signal is also acquired (Fig. 3(d)), which may be induced by the diffusion of Cr from HEA to the surface nanostructures during the OER activation process. For the Ni elements, except for the hydroxides (Ni-OH: 855.7 eV) and sulfates (857.5 eV), the new peaks of oxides (Ni-O: 855 and 856.5 eV) [20] can also be detected (Fig. 3(e)). The S signal becomes very weak after CV cycles (Fig. 3(g)), because KOH reacts with the sulfates. In addition, the new M-O signal (529.6 eV) is also detected in the O 1s spectra, except those for M-OH (530.9 eV) and M-SO$_4$ (532.0 eV) (Fig. 3(f)). Compared to HEA-250Ni, the oxides are formed and the sulfates are reduced after CV activation, indicating the surface reconstruction in the OER process.

3.5. OER performance

The OER activities of Fe$_{50}$Mn$_{30}$Co$_{10}$Cr$_{10}$ treated by different sulfates and various concentrations of NiSO$_4$ were investigated and compared with those of pristine NF and HEA in 1 M KOH through a typical three-electrode system. The HEA-250Ni displays the best catalytic activity with overpotentials as low as 247, 313, and 362 mV to achieve 10, 50, and 100 mA cm^{-2}, respectively, which are much lower than those of HEA (346, 444, and 518 mV) and NF (380, 454, and 493 mV) (Figs. 4(a) and S4, and Table S1 in Supporting Information). The concentration of NiSO$_4$ has little effect on the OER performance at the low current densities (below 50 mA cm^{-2}). While, the OER performance at the high current densities (over 50 mA cm^{-2}) is enhanced obviously as the concentration increasing from 100 mM to 250 mM, and reduced with further increasing the concentration (Fig. S5 and Table S1 in supporting information). The oxidation–reduction (redox) reaction in the OER process becomes more intensive as the concentration of NiSO$_4$ increases, indicating more low-valence metal ions are oxidized to high-valence states on the HEA surface (Fig. S5, supporting information). The redox waves shift toward the lower potential could be derived from the active-site formation for OER and microstructural changes of the surface hydroxide films (Fig. S5, supporting information) [54]. From the SEM images, we see that HEA-250Ni has a uniform layer of honeycomb nanostructures, which may lead to a high specific surface area with rich active sites. We also see that different sulfates have different effects on the OER performance, and HEA-250Ni has the lowest overpotentials at both low and high current densities (Fig. S6 and Table S1 in Supporting Information). The intensity and location of the redox waves also change under different sulfates, indicating that the sulfates affect the oxidization of the low-valent metal ions to high-valent states on the HEA surface, the active-site formation for OER, and microstructure of the surface hydroxide film (Fig. S6, supporting information). The OER

performance of HEA-125Ni-125Fe is better than that of HEA-250Fe, and the OER performance of HEA-125Ni-125Co is better than that of HEA-250Co, indicating the addition of Ni plays more important role than other elements in improving OER performance. NiSO$_4$ is the best corrosion solution among the considered sulfates because of the following reasons. (1) The hydroxides containing Ni has higher OER activity than other hydroxides. (2) The HEA corroded in NiSO$_4$ solution is easier to form the uniform honeycomb nanostructure than that in other solutions. (3) The HEA corroded in NiSO$_4$ solution could form honeycomb nanostructure with small size, which provides more activity sites than that in other solutions. Clearly, the HEA corroded by sulfates exhibits remarkable electrocatalytic activity for OER (Fig. S4–S6 and Table S1, supporting information), confirming that corrosion engineering is an effective way to transform the inexpensive HEA into highly efficient OER electrocatalyst.

To figure out the mechanism, the reaction kinetics was investigated. We see that HEA-250Ni exhibits a very small Tafel slope of 63 mV dec^{-1}, which is superior to those of HEA (97 mV dec^{-1}) and NF (94 mV dec^{-1}), indicating its intrinsic excellent OER activity and the fast charge transfer in the reaction (Fig. 4(b)). As the Tafel slope is around 60 mV dec^{-1}, the OER for HEA-250Ni is limited by the first electron/proton reaction, i.e., the adsorption and energy optimization of OH reactants (M+OH→M-OH+e^- together with M-OH→M-OH*, where M represents the catalytic active site) [55]. Importantly, the catalytic performance of HEA-250Ni is much better than most of the HEA-based prepared by other methods [37,56,57] and the commercial RuO$_2$ powder [9], and is similar to or even better than those of most LDH powders [58–60], and LDH on NF (Ni Foam) [61], CFP (carbon fiber paper) [62], or other substrates (stainless-steel) [54,63], and other alloy [64] (Table S2 in supporting information).

To further reveal the origin of the enhanced activity, it is necessary to evaluate the exposed active sites by the electrochemical active surface area (ECSA) [65]. The ECSA value is related to the double-layer capacitance (C_{dl}) [66], which can be measured by the CV tests under different scan rates in a non-Faradic potential (Fig. S7, supporting information). The C_{dl} values of NF, HEA, and HEA-250Ni are 1.74, 11.6, and 13.1 mF cm^{-2}, respectively, indicating that HEA-250Ni has the highest active sites to boost the OER activity (Fig. 4(c)). Electrochemical impedance spectroscopy (EIS) was used to evaluate the catalytic kinetics of catalysts (Fig. 4(d)). HEA-250Ni has a R_{ct} (charge transfer resistance) of 1.27 Ω, which is much lower than that of HEA (5.7 Ω) and NF (20.5 Ω), indicating faster electron-transfer kinetics, which further confirms its high inherent catalytic activity.

The long-term stability of the catalysts is also one of the important factors for practical application. The durability of HEA-250Ni was tested by carrying out LSV cycling and monitoring the current density at the constant voltage in 1 M KOH. The difference in the LSV curves of the HEA-250Ni catalyst between the initial and after 2000 cycles is negligible under both with and without *iR* correction (Figs. 4(e) and S8 in Supporting Information). The electrocatalytic stability was further investigated by chronoamperometric (I-t) test without *iR* correction in 1 M KOH (Fig. 4(f)). The current density of 100 mA cm^{-2} at a constant overpotential (420 mV) shows a negligible decrease for 60 h, indicating that HEA-250Ni has excellent stability under high current density in 1 M KOH.

3.6. Structure and morphology of the HEA after OER

The morphology, structure, surface composition, and chemical states of HEA-250Ni after the OER long-term stability test were characterized by SEM, TEM, XRD, Raman scattering and XPS to further reveal the origin of excellent OER catalytic activity and confirm the stability (Figs. 5 and S9–11 in supporting information).
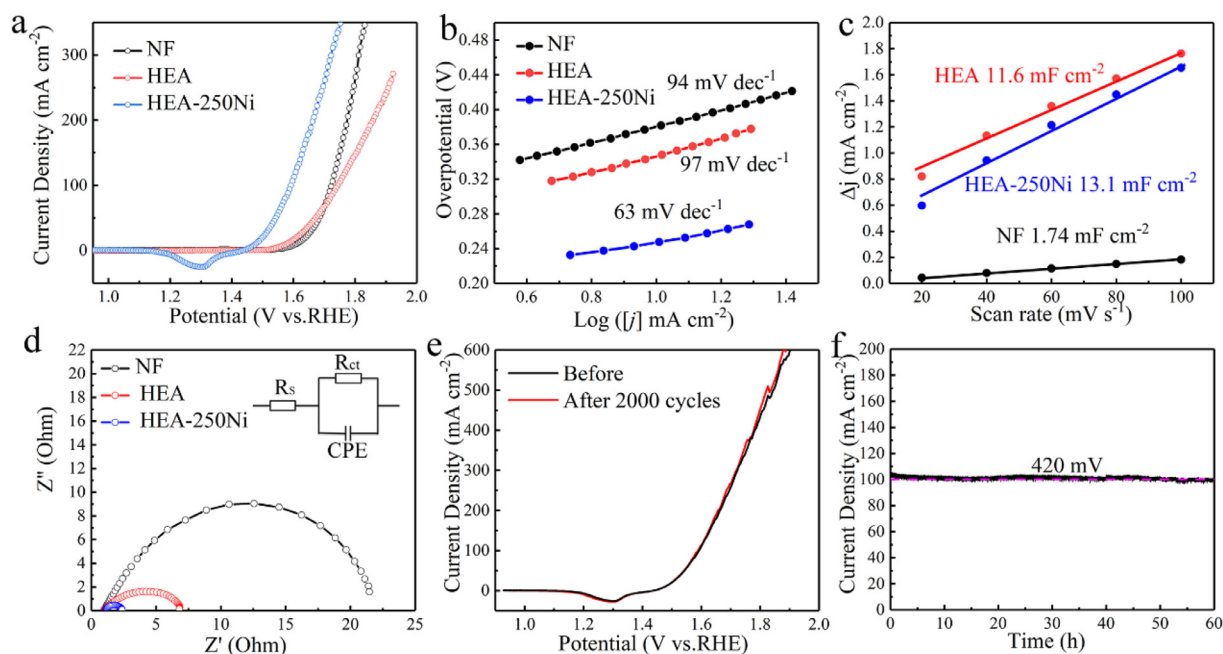
Fig. 4. (a) OER linear sweep voltammetry curves with *iR* compensation, (b) Tafel slope, and (c) the double-layer capacitances (C_{dl}), and (d) the electrochemical impedance spectroscopies (EIS) and the equivalent circuit (inset) of Ni foam, HEA, and HEA-250Ni in 1 M KOH solution. (e) The cycle stability with *iR* correction for HEA-250Ni, and (f) time dependence of current density under constant potential without *iR* correction for HEA-250Ni.

The XRD patterns show that no new phase formed after the stability test due to the detection limit too (Fig. S9(a), supporting information). However, the Raman spectra shows that the peaks of M-OH (453 and 532 cm^{-1}, blue lines) are still there, while the peak at 248 cm^{-1} disappears (Fig. 5(c)). At the same time, we see that the M–O peaks (green lines) are observed, and the sulfate peaks disappear, indicating the formation of oxides and the dissolution of sulfates during the long-term stability OER test (Fig. 5(c)). The Raman results show that there is surface reconstruction during the OER process. The sample after the long-term stability test still keeps the honeycomb structure with some particles covered on its surface and the wall of the honeycomb becomes thicker (Fig. S10(a) and (b), Supporting Information). Differently, the crystallinity of the sample is greatly improved after the long-term test (Fig. 5(a) and (b)), further confirming the reconstruction of the nanostructure on the surface in the OER process. In addition, the HADDF-STEM images and EDS mappings show that the catalyst is mainly composed of Fe, Mn, Co, Ni, and O after the long-term test, while S and Cr cannot be detected (Fig. S10(e), supporting information). The XPS results further confirm the reconstruction of the nanostructure on the surface (Figs. 5(d)–(j)). For the Fe, Co, and Ni elements, three peaks are observed, corresponding to oxides (Fe-O: 712.2 eV; Co-O: 780 and 778.9 eV; Ni-O: 857 and 855 eV; blue lines), hydroxides (Fe-OH: 710.2 eV; Co-OH: 781.5 eV; Ni-OH: 855.7 eV; pink lines) and the satellites (green lines). For the Mn element, the weak Mn metal peak (638.3 eV; red line) is still there, except for Mn-OH (643.1 eV; pink line) and Mn-O (641.8 eV; blue line). In these elements, no sulfate peak is observed due to its dissolution. Compared to the catalyst after 500 cycles CV activation, the XPS peaks of hydroxides for Fe, Mn, Co, and Ni have almost no change, while those of oxides change obviously (Fig. S11, Supporting Information). The oxide peaks of Fe and Mn shift toward high binding energy by 0.5 and 0.7 eV, respectively (Fig. S11(a) and (b), supporting information). The Ni-O peak at 856.5 eV shifts to high binding energy by 0.5 eV and another peak does not change (Fig. S11(e), supporting information). The positive shift demonstrates that the metal valence state of oxides is increased during the OER process. The main

Co-O peak does not move, but a new Co-O peak in low energy occurs, indicating that the high-valence cobalt oxide is formed (Fig. S11(c), supporting information). Consequently, the M-O at 529.1 eV has a negative shift in the O 1s XPS spectrum after the stability test, which indicates extensive charge transfer to lattice metal-O (Fig. S11(f), supporting information) [20,67–69]. The peak of M-OH at 530.7 eV shifts negatively by 0.2 eV after the stability test, which also confirms that the metal valence state is increased. In addition, the intensity of XPS peaks for oxides increases, while those for hydroxides decreases, showing that the hydroxides transform to oxides during the long-term OER test. The S signal is not detected, further confirming that the sulfates react with KOH during the OER process (Fig. S11(g), supporting information). Similarly, no Cr signal is detected because Cr^{3+} in hydroxides dissolves into the strong alkaline electrolyte ($Cr(OH)_3+OH^- \rightarrow [Cr(OH)_4]^-$) in the stability test (Fig. S11(d), supporting information) [70].

Our findings show that the catalytic performance of HEA is promoted by the corrosion engineering, and the corrosive solution needs to be carefully chosen for the purpose. For the improved performance, there are a few factors that need to be considered. Firstly, HEA-250Ni is composed of binder-free self-supported honeycomb nanostructures and multi-component hydroxides. The honeycomb nanostructure is beneficial for avoiding the irregular aggregation of active phases and exposing the active sites as much as possible, as indicated by the high ECSA data (Fig. 4(c)). The binder-free self-supported structure leads to the intimate connection between the hydroxides and HEA substrate, further reducing the interfacial resistance between them, as confirmed by the EIS result (Fig. 4(d)) [43]. Most importantly, the hydroxides strongly adhere to the HEA substrate, which avoids the catalytically active phases peeling off during the OER process, leading to high stability (Fig. 4(e) and (f)). Additionally, the multi-metal hydroxides can enhance the intrinsic activity due to the synergistic effect of multi-metal hydroxides, resulting in a low Tafel slope (Fig. 4(b)) [41,71]. Secondly, the metal elements in HEA-250Ni have high valence states. During the OER process, the phase transformation from the hydroxides to oxides shows that the valence states of
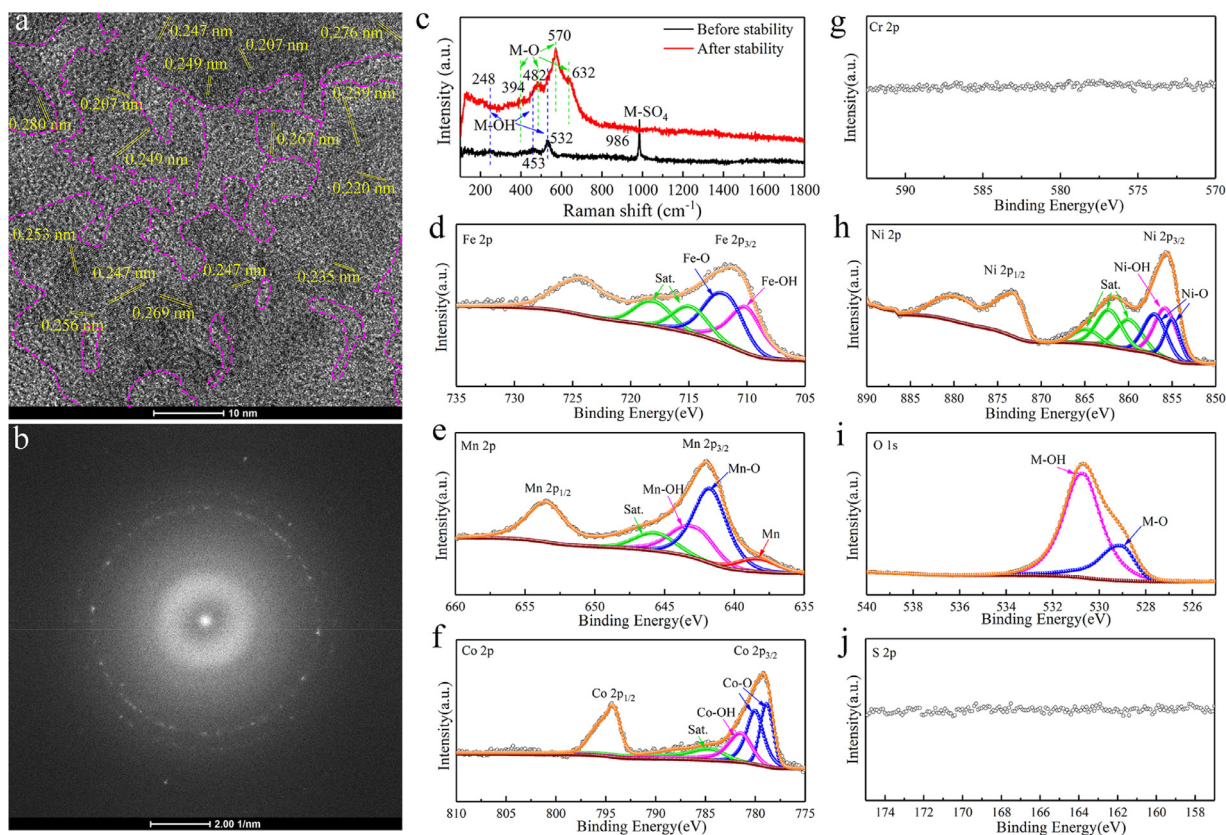
Fig. 5. (a) HRTEM image, (b) SAED pattern, (c) Raman spectra, and High-resolution XPS spectra of (d) Fe 2p, (e) Mn 2p, (f) Co 2p, (g) Cr 2p, (h) Ni 2p, (i) O 1s, and (j) S2p for HEA-250Ni after the stability test.

the metal elements are increased. The multiple valence states provide tremendous intermediates and active sites, leading to reduced kinetic barriers [72]. At the same time, 3d transition metals with high-valence states much more easily absorb polarized molecules, which enhances the electrophilicity of the adsorbed O, and thus facilitates the reaction of an OH^- anion with an adsorbed O atom on the catalytic active site, leading to the easy formation of adsorbed OOH species for the fast OER process [62,72–74]. Additionally, the interface between the hydroxides and oxides [54,75], and the pores formed due to the dissolution of Cr can also help improve the OER performance [70].

4. Conclusion

In summary, a simple corrosion engineering method has been used to prepare the self-supported 3D printed $Fe_{50}Mn_{30}Co_{10}Cr_{10}$ HEA as the catalyst for OER. We find that HEA-250Ni exhibits an ultrahigh OER electrocatalytic performance with an exceptionally small overpotential at a variety of current densities and excellent long-term stability in 1 M KOH. The overpotentials to achieve a current density of 10, 50, and 100 mA cm^{-2} are ~247, ~313, and ~362 mV, respectively, which are lower than those of most reported values for the state-of-art materials. The excellent OER performance is contributed by: (1) the special honeycomb nanostructure, which exposes abundant active sites; (2) the multi-metal hydroxides, which enhance the intrinsic activity due to the synergistic effect; (3) the binder-free self-supported structure, which reduces interfacial resistance; and (4) the multiple valence states, which improve the reaction kinetics. Our work offers a practical and effective way to prepare high-performance, low-cost, and large-scale electrocatalysts for OER. We believe that the OER performance of HEA could be further improved by adjusting the 3D

printing parameters to prepare the porous bulk alloy, which may open up a new avenue to prepare large-scale HEA by 3D printing and corrosion engineering as electrocatalysts and guide the design of novel catalysts for industrial applications.

Declaration of Competing Interest

There are no conflicts to declare.

Supplementary materials

Supplementary material associated with this article can be found, in the online version, at doi:10.1016/j.jmst.2021.09.003.

References

[1] K. Wu, X. Wei, D. Li, P. Hu, J. Mater. Sci. Technol. (2021), doi:10.1016/j.jmst.2021.01.091.
[2] M. Ramadoss, Y. Chen, Y. Hu, B. Wang, R. Jeyagopal, K. Marimuthu, X. Wang, D. Yang, J. Mater. Sci. Technol. 78 (2021) 229–237.
[3] T. Liu, D. Liu, F. Qu, D. Wang, L. Zhang, R. Ge, S. Hao, Y. Ma, G. Du, A.M. Asiri, L. Chen, X. Sun, Adv. Energy Mater. 7 (2017) 201700020.
[4] W.J. Ong, N. Zheng, M. Antonietti, Nanoscale 13 (2021) 9904–9907.
[5] X. Shang, J.H. Tang, B. Dong, Y. Sun, Sustain. Energy Fuels 4 (2020) 3211–3228.
[6] S. Xu, H. Zhao, T. Li, J. Liang, S. Lu, G. Chen, S. Gao, A.M. Asiri, Q. Wu, X. Sun, J. Mater. Chem. A 8 (2020) 19729–19745.

[7] Y. Wang, S. Tao, H. Lin, G. Wang, K. Zhao, R. Cai, K. Tao, C. Zhang, M. Sun, J. Hu, B. Huang, S. Yang, Nano Energy 81 (2021) 105606.

[8] L. Zhang, H. Zhao, S. Xu, Q. Liu, T. Li, Y. Luo, S. Gao, X. Shi, A.M. Asiri, X. Sun, Small Struct. 2 (2020) 202000048.

[9] X. Du, H. Ai, M. Chen, D. Liu, S. Chen, X. Wang, K.H. Lo, H. Pan, Appl. Catal. B Environ. 272 (2020) 119046.

[10] J. Liu, T. Zhang, G.I.N. Waterhouse, J. Mater. Chem. A 8 (2020) 23142–23161.

[11] X. Ren, Y. Zhai, Q. Zhou, J. Yan, S. Liu, J. Energy Chem. 50 (2020) 125–134.

[12] C. Kim, S.H. Kim, S. Lee, I. Kwon, S.H. Kim, S. Kim, C. Seok, Y.S. Park, Y. Kim, J. Energy Chem. 64 (2022) 364–371.

[13] J. Zhang, J. Liu, L. Xi, Y. Yu, N. Chen, S. Sun, W. Wang, K.M. Lange, B. Zhang, J. Am. Chem. Soc. 140 (2018) 3876–3879.

[14] Y. Cao, T. Wang, X. Li, L. Zhang, Y. Luo, F. Zhang, A.M. Asiri, J. Hu, Q. Liu, X. Sun, Inorg. Chem. Front. 8 (2021) 3049–3054.

[15] C. Ye, L. Zhang, L. Yue, B. Deng, Y. Cao, Q. Liu, Y. Luo, S. Lu, B. Zheng, X. Sun, Inorg. Chem. Front. 8 (2021) 3162–3166.

[16] J.Y. Zhang, L. Lv, Y. Tian, Z. Li, X. Ao, Y. Lan, J. Jiang, C. Wang, ACS Appl. Mater. Interfaces 9 (2017) 33833–33840.

[17] C. Yan, J. Huang, C. Wu, Y. Li, Y. Tan, L. Zhang, Y. Sun, X. Huang, J. Xiong, J. Mater. Sci. Technol. 42 (2020) 10–16.

[18] Y. Pang, W. Xu, S. Zhu, Z. Cui, Y. Liang, Z. Li, S. Wu, C. Chang, S. Luo, J. Mater. Sci. Technol. 82 (2021) 96–104.

[19] G. Tian, S. Wei, Z. Guo, S. Wu, Z. Chen, F. Xu, Y. Cao, Z. Liu, J. Wang, L. Ding, J. Tu, H. Zeng, J. Mater. Sci. Technol. 77 (2021) 108–116.

[20] D. Liu, H. Ai, J. Li, M. Fang, M. Chen, D. Liu, X. Du, P. Zhou, F. Li, K.H. Lo, Y. Tang, S. Chen, L. Wang, G. Xing, H. Pan, Adv. Energy Mater. 10 (2020) 2002464.

[21] L. Wu, L. Yu, X. Xiao, F. Zhang, S. Song, S. Chen, Z. Ren, Research 2020 (2020) 3976278 (Washington DC).

[22] P.F. Zhou, D.H. Xiao, Z. Wu, X.Q. Ou, Mater. Sci. Eng. A 739 (2019) 86–89.

[23] Z. Li, K.G. Pradeep, Y. Deng, D. Raabe, C.C. Tasan, Nature 534 (2016) 227–230.

[24] D.B. Miracle, Mater. Sci. Technol. 31 (2015) 1142–1147.

[25] J. Gao, Y. Jin, Y. Fan, D. Xu, L. Meng, C. Wang, Y. Yu, D. Zhang, F. Wang, J. Mater. Sci. Technol. 102 (2022) 159–165.

[26] Z. He, N. Jia, H. Wang, H. Yan, Y. Shen, J. Mater. Sci. Technol. 86 (2021) 158–170.

[27] J. Xu, X. Kong, M. Chen, Q. Wang, F. Wang, J. Mater. Sci. Technol. 82 (2021) 207–213.

[28] S. Chang, X. Huang, C.Y. Aaron Ong, L. Zhao, L. Li, X. Wang, J. Ding, J. Mater. Chem. A 7 (2019) 18338–18347.

[29] P. Ma, S. Zhang, M. Zhang, J. Gu, L. Zhang, Y. Sun, W. Ji, Z. Fu, Sci. China Mater. 63 (2020) 2613–2619.

[30] G.M. Tomboc, T. Kwon, J. Joo, K. Lee, J. Mater. Chem. A 8 (2020) 14844–14862.

[31] H. Li, Y. Han, H. Zhao, W. Qi, D. Zhang, Y. Yu, W. Cai, S. Li, J. Lai, B. Huang, L. Wang, Nat. Commun. 11 (2020) 5437.

[32] J. Huang, P. Wang, P. Li, H. Yin, D. Wang, J. Mater. Sci. Technol. 93 (2021) 110–118.

[33] X. Wang, Q. Dong, H. Qiao, Z. Huang, M.T. Saray, G. Zhong, Z. Lin, M. Cui, A. Brozena, M. Hong, Q. Xia, J. Gao, G. Chen, R. Shahbazian-Yassar, D. Wang, L. Hu, Adv. Mater. 32 (2020) e2002853.

[34] N.L.N. Broge, M. Bondesgaard, F. Sondergaard-Pedersen, M. Roelsgaard, B.B. Iversen, Angew. Chem. Int. Ed. Engl. 59 (2020) 21920–21924.

[35] M. Bondesgaard, N.L.N. Broge, A. Mamakhel, M. Bremholm, B.B. Iversen, Adv. Funct. Mater. 29 (2019) 1905933.

[36] H. Peng, Y. Xie, Z. Xie, Y. Wu, W. Zhu, S. Liang, L. Wang, J. Mater. Chem. A 8 (2020) 18318–18326.

[37] W. Dai, T. Lu, Y. Pan, J. Power Sources 430 (2019) 104–111.

[38] S. Gupta, S. Zhao, X.X. Wang, S. Hwang, S. Karakalos, S.V. Devaguptapu, S. Mukherjee, D. Su, H. Xu, G. Wu, ACS Catal. 7 (2017) 8386–8393.

[39] S. Li, X. Tang, H. Jia, H. Li, G. Xie, X. Liu, X. Lin, H.J. Qiu, J. Catal. 383 (2020) 164–171.

[40] H.J. Qiu, G. Fang, J. Gao, Y. Wen, J. Lv, H. Li, G. Xie, X. Liu, S. Sun, ACS Mater. Lett. 1 (2019) 526–533.

[41] G. Fang, J. Gao, J. Lv, H. Jia, H. Li, W. Liu, G. Xie, Z. Chen, Y. Huang, Q. Yuan, X. Liu, X. Lin, S. Sun, H.J. Qiu, Appl. Catal. B Environ. 268 (2020) 118431.

[42] X. Cui, B. Zhang, C. Zeng, S. Guo, MRS Commun. 8 (2018) 1230–1235.

[43] Y. Liu, X. Liang, L. Gu, Y. Zhang, G.D. Li, X. Zou, J.S. Chen, Nat. Commun. 9 (2018) 2609.

[44] V.R. Jothi, K. Karuppasamy, T. Maiyalagan, H. Rajan, C.Y. Jung, S.C. Yi, Adv. Energy Mater. 10 (2020) 1904020.

[45] X. Liu, M. Gong, S. Deng, T. Zhao, T. Shen, J. Zhang, D. Wang, Adv. Funct. Mater. 31 (2020) 2009032.

[46] X. Zhao, Y. Su, S. Li, Y. Bi, X. Han, J. Environ. Sci. 73 (2018) 47–57 (China).

[47] W. Chen, G. Qian, Q. Xu, C. Yu, M. Yu, Y. Xia, S. Yin, Nanoscale 12 (2020) 7116–7123.

[48] J. Baltrusaitis, D.M. Cwiertny, V.H. Grassian, Phys. Chem. Chem. Phys. 9 (2007) 5542–5554.

[49] S. Anantharaj, M. Venkatesh, A.S. Salunke, T.V.S.V. Simha, V. Prabu, S. Kundu, A.C.S. Sustain, Chem. Eng. 5 (2017) 10072–10083.

[50] F. Jin, H. Long, W. Song, G. Xiong, X. Guo, X. Wang, Energy Fuels 27 (2013) 3394–3399.

[51] M.A.Z.G. Sial, S. Baskaran, A. Jalil, S.H. Talib, H. Lin, Y. Yao, Q. Zhang, H. Qian, J. Zou, X. Zeng, Int. J. Hydrog. Energy 44 (2019) 22991–23001.

[52] M.Y. Wang, C.J. Jiang, X.W. Wang, P.F. Xian, H.G. Wang, Y. Yang, Rare Met. 36 (2015) 612–616.

[53] J. Sicklinger, H. Beyer, L. Hartmann, F. Riewald, C. Sedlmeier, H.A. Gasteiger, J. Electrochem. Soc. 167 (2020) 130507.

[54] N. Todoroki, T. Wadayama, ACS Appl. Mater. Interfaces 11 (2019) 44161–44169.

[55] J. Park, Y.J. Sa, H. Baik, T. Kwon, S.H. Joo, K. Lee, ACS Nano 11 (2017) 5500–5509.

[56] H. Liu, C. Xi, J. Xin, G. Zhang, S. Zhang, Z. Zhang, Q. Huang, J. Li, H. Liu, J. Kang, Chem. Eng. J. 404 (2021) 126530.

[57] H. Wang, R. Wei, X. Li, X. Ma, X. Hao, G. Guan, J. Mater. Sci. Technol. 68 (2021) 191–198.

[58] F. Li, Z. Sun, H. Jiang, Z. Ma, Q. Wang, F. Qu, Energy Fuels 34 (2020) 11628–11636.

[59] Z. Li, Q. Qian, Y. Tian, Y. Li, X. Sun, X. Duan, Chem. Commun 52 (2016) 908–911 (Camb).

[60] Q. Zhou, Y. Chen, G. Zhao, Y. Lin, Z. Yu, X. Xu, X. Wang, H.K. Liu, W. Sun, S.X. Dou, ACS Catal. 8 (2018) 5382–5390.

[61] R. Fan, Q. Mu, Z. Wei, Y. Peng, M. Shen, J. Mater. Chem. A 8 (2020) 9871–9881.

[62] Y. Yang, Y. Song, S. Mo, M. Liu, Chem. Eng. J. 417 (2020) 127934.

[63] M. Cai, W. Liu, X. Luo, C. Chen, R. Pan, H. Zhang, M. Zhong, ACS Appl. Mater. Interfaces 12 (2020) 13971–13981.

[64] W. Li, Q. Hu, Y. Liu, M. Zhang, J. Wang, X. Han, C. Zhong, W. Hu, Y. Deng, J. Mater. Sci. Technol. 37 (2020) 154–160.

[65] C. Liang, P. Zou, A. Nairan, Y. Zhang, J. Liu, K. Liu, S. Hu, F. Kang, H.J. Fan, C. Yang, Energy Environ. Sci. 13 (2020) 86–95.

[66] M. Kuang, P. Han, Q. Wang, J. Li, G. Zheng, Adv. Funct. Mater. 26 (2016) 8555–8561.

[67] Z. Chen, L. Cai, X. Yang, C. Kronawitter, L. Guo, S. Shen, B.E. Koel, ACS Catal. 8 (2018) 1238–1247.

[68] J.C. Dupin, D. Gonbeau, P. Vinatier, A. Levasseur, Phys. Chem. Chem. Phys. 2 (2000) 1319–1324.

[69] L. Yu, Q. Zhu, S. Song, B. McElhenny, D. Wang, C. Wu, Z. Qin, J. Bao, Y. Yu, S. Chen, Z. Ren, Nat. Commun. 10 (2019) 5106.

[70] X. Bo, Y. Li, R.K. Hocking, C. Zhao, ACS Appl. Mater. Interfaces 9 (2017) 41239–41245.

[71] W.J. Jiang, T. Tang, Y. Zhang, J.S. Hu, Acc. Chem. Res. 53 (2020) 1111–1123.

[72] Z. Ding, J. Bian, S. Shuang, X. Liu, Y. Hu, C. Sun, Y. Yang, Adv. Sustain. Syst. 4 (2020) 1900105.

[73] Z. Dai, H. Geng, J. Wang, Y. Luo, B. Li, Y. Zong, J. Yang, Y. Guo, Y. Zheng, X. Wang, Q. Yan, ACS Nano 11 (2017) 11031–11040.

[74] A. Grimaud, K.J. May, C.E. Carlton, Y.L. Lee, M. Risch, W.T. Hong, J. Zhou, Y. Shao-Horn, Nat. Commun. 4 (2013) 2439.

[75] Y. Wang, T. Wang, R. Zhang, Q. Liu, Y. Luo, G. Cui, S. Lu, J. Wang, Y. Ma, X. Sun, Inorg. Chem. 59 (2020) 9491–9495.